The Astrophysical Journal, 909:10 (11pp), 2021 March 1 https://doi.org/10.3847/1538-4357/abd6e6

Effects of Pseudostreamer Boundary Dynamics on Heliospheric Field and Wind

V. Aslanyan[1], D. I. Pontin[2], P. F. Wyper[3], R. B. Scott[4], S. K. Antiochos[5], and C. R. DeVore[5]
[1] School of Mathematics, University of Dundee, Dundee, DD1 4HN, UK; vaslanyan001@dundee.ac.uk
[2] School of Mathematical and Physical Sciences, University of Newcastle, University Drive, Callaghan, NSW 2308, Australia
[3] Department of Mathematical Sciences, Durham University, Durham DH1 3LE, UK
[4] NRC Research Associate at The U.S. Naval Research Laboratory, Washington, DC 20375, USA
[5] Heliophysics Science Division, NASA Goddard Space Flight Center, Greenbelt, MD 20771, USA
Received 2020 December 8; revised 2020 December 22; accepted 2020 December 24; published 2021 March 1

Abstract

Interchange reconnection has been proposed as a mechanism for the generation of the slow solar wind, and a key contributor to determining its characteristic qualities. In this paper we study the implications of interchange reconnection for the structure of the plasma and field in the heliosphere. We use the Adaptively Refined Magnetohydrodynamic Solver to simulate the coronal magnetic evolution in a coronal topology containing both a pseudostreamer and helmet streamer. We begin with a geometry containing a low-latitude coronal hole that is separated from the main polar coronal hole by a pseudostreamer. We drive the system by imposing rotating flows at the solar surface within and around the low-latitude coronal hole, which leads to a corrugation (at low altitudes) of the separatrix surfaces that separate open from closed magnetic flux. Interchange reconnection is induced both at the null points and separators of the pseudostreamer, and at the global helmet streamer. We demonstrate that a preferential occurrence of interchange reconnection in the "lanes" between our driving cells leads to a filamentary pattern of newly opened flux in the heliosphere. These flux bundles connect to but extend far from the separatrix-web (S-Web) arcs at the source surface. We propose that the pattern of granular and supergranular flows on the photosphere should leave an observable imprint in the heliosphere.

Unified Astronomy Thesaurus concepts: Slow solar wind (1873); Solar magnetic reconnection (1504); Magnetohydrodynamics (1964); Solar corona (1483)

1. Introduction

Solar wind is characterized as "fast," with typical plasma speeds >500 km s^{-1} or otherwise as "slow," with the latter exhibiting transient behavior and compositional differences (e.g., Abbo et al. 2016). While the fast wind is known to originate directly from coronal holes, where open magnetic field lines extend away from the Sun, the processes responsible for determining the nature of the slow wind remain the subject of ongoing investigation. One mechanism that is proposed to play an important role is interchange reconnection between "closed" and "open" field lines, which can release plasma confined on the former to escape along the latter. Closed coronal field lines begin and end at two points on the photosphere and, therefore, have finite length; whereas, open field lines begin at the photosphere and extend out indefinitely into the heliosphere. Reconnection can occur entirely in the open-field region, entirely in the closed-field region, or at the boundary between open and closed magnetic flux, the latter being termed "interchange reconnection" (Crooker et al. 2002). Such a process can therefore occur only where the open and closed field lines are adjacent to one another. This is the central premise behind the separatrix-web (S-web) model (Antiochos et al. 2011), which invokes interchange reconnection to argue that slow wind should be found on the web of open flux tubes immediately adjacent to the closed-field corona. The broad latitudinal extent of the S-web then provides a natural explanation for the extent of slow solar wind on the scale of the entire Sun. Our aim in this paper is to explore the expected observable signatures of interchange reconnection in a pseudostreamer geometry in the presence of photospheric driving that mimics supergranulation.

The solar magnetic field can be calculated and understood through the Potential Field Source Surface model. In the case of both a priori magnetic geometries and extrapolations of observational data, the source surface mimics the effect of the solar wind that drags field lines out to fill the heliosphere.

Observationally, the boundary between open and closed magnetic flux is presumed to coincide with the boundaries of coronal holes; dark regions in coronal emission where the plasma density is low (Cranmer 2009). The correlation is generally good—however, the boundaries of coronal holes are difficult to precisely define, due to a number of complicating factors including obscuration by neighboring closed flux that depends on the line of sight. Indeed, the boundaries of coronal holes often appear "fuzzy" or "ragged" rather than well-defined transitions (Kahler & Hudson 2002). One natural explanation is that the plasma is highly dynamic in these regions: continual interchange reconnection leads to a transport of dense plasma into the open-field region (and tenuous plasma into the closed-field region). If this happens continuously over a range of scales (as expected during bursty reconnection at coronal plasma parameters, e.g., Karpen et al. 2012; Pontin & Wyper 2015; Wyper et al. 2016) it can be expected to result in a gradient in plasma properties across a boundary layer of finite width (averaged over a suitable time period), rather than a sharp transition between "open-field plasma" and "closed-field plasma." Moreover, the boundary between open and closed flux itself can be expected to be much less geometrically regular than in potential field or force-free field extrapolations.

As we show below, we should expect a corrugation of the surface that forms the open–closed boundary whose length scale is inherited from the photospheric driving.

Theoretically, the boundary between open and closed magnetic flux is presumed to define separatrices associated with the heliospheric current sheet (i.e., the global helmet streamer) as well as the plethora of coronal magnetic nulls and (to a lesser extent) bald patches (Titov et al. 2011; Platten et al. 2014; Scott et al. 2018, 2019). In order to assess the implications of interchange reconnection for the solar wind, we need to understand how the process evolves at these various structures, and how it relates to different features of the observations (Viall & Borovsky 2020). Here we consider one typical coronal geometry: a pseudostreamer (Wang et al. 2007) that separates coronal holes of the same magnetic polarity. Such pseudostreamers appear abundantly in observations, such as EUV images of the low corona (Masson et al. 2014). In order to explain such a structure, the corresponding magnetic field geometry must exhibit certain features. First, at low heights a separatrix surface must distinguish the open field lines in the coronal holes from the closed flux that separates them. Second, at large heights a separatrix surface must partition the flux of one coronal hole from the other. Thus, the magnetic field of the pseudostreamer is composed of multiple separatrices associated with coronal null points and possibly bald patches (Titov et al. 2011). In a survey of coronal potential field models, Scott et al. (2019) found that around half of all arc features of the S-Web are composed of such separatrices associated with coronal nulls—the other half being associated with the narrow corridors of open flux first discussed by Antiochos et al. (2011). This motivates the study of interchange reconnection in each of these different scenarios. Interchange reconnection in a narrow corridor of open flux was addressed in the studies of Higginson et al. (2017a, 2017b).

The S-Web model reveals that the heliospheric magnetic field is threaded by an array of surfaces that correspond to separatrices or quasi-separatrix layers (QSLs), these surfaces defining locations at which open flux passes close to closed flux in the inner corona. New in situ data from the Parker Solar Probe (PSP) promises the opportunity for direct measurements of the fields and plasma parameters in the vicinity of S-Web structures associated, for example, with pseudostreamers. In this paper we make a first step toward a modeling prediction for the in situ observable signatures by the PSP of interchange reconnection in the low corona.

In the following section we introduce a magnetic field model containing a pseudostreamer and low-latitude coronal hole that forms the basis of our study. In Section 3 we explore the different patterns that could be expected for interchange-reconnected flux at large altitudes. We then go on to test these in dynamical MHD simulations described in Sections 4 and 5. We finish with a conclusion in Section 6.

2. Magnetic Geometry

We base our investigation on a magnetic configuration that has been analyzed in previous (static) topological studies of the S-Web by Titov et al. (2011). The model field includes an extended region of parasitic polarity in one hemisphere. Containing the flux of the parasitic polarity is a magnetic separatrix "dome" with the characteristics of a pseudostreamer, which partitions the flux in the polar coronal hole from a low-latitude coronal hole of the same polarity (see Figure 1). The simulation domain extends radially from the photosphere at $R_\odot$ to $3R_\odot$, covering polar angles θ between $\pm 79°$, and all azimuthal angles ϕ. The magnetic field within this domain is initially computed using the standard Potential Field Source Surface model (Altschuler & Newkirk 1969; Schatten et al. 1969). This model mimics the effect of the solar wind that drags field lines out to fill the heliosphere by enforcing that the field is purely radial at the outer boundary, the so-called source surface. The field in the domain volume defined by the photosphere and the source surface is assumed to be potential.

We calculated the magnetostatic potential for this field using a decomposition into spherical harmonics, with the dominant component being the global solar dipole, with a field strength of 10 G at the poles on the photosphere. The northern coronal hole is extended southwards to form the commonly observed "elephant-trunk" configuration (Zirker 1977) by adding a dipole (representative of a large bipolar active region) close to the equator. A pseudostreamer is then formed by the addition of four, relatively weak, narrowly spaced dipoles, bounding the isolated coronal hole from the north. The resulting photospheric and coronal magnetic field geometries are shown in Figure 1. The flux of the mid-latitude coronal hole—whose center lies at $\theta \sim 20$ and $\phi \sim 0$ at the photosphere—is bounded to the south by the global helmet streamer. To the north, the flux is bounded by a magnetic "dome" structure and vertical separatrix curtain, these being composed of the separatrix surfaces of the coronal null points (field lines within the dome are colored green in Figures 1(a) and (e)). The dome of the pseudostreamer encloses an area 4.1×10^5 Mm^2 (6.6% of the total) at the photosphere and extends a distance approximately 180 Mm ($\sim 0.25R_\odot$) above the photosphere (the approximate height of the coronal nulls); the peak radial field strength at the photosphere beneath the pseudostreamer dome is 42 G, with a total magnetic flux of 4.7×10^6 G Mm^2. Full details of the dipole strengths that define the initial condition are given in the Appendix.

To analyze and visualize the coronal magnetic field structure, we make use of the squashing factor Q, calculated efficiently using the GPU-compatible QSL Squasher code (Tassev & Savcheva 2017). The squashing factor is a measure of the complexity of the magnetic field line mapping between two boundaries. Considering an infinitesimal flux tube of circular cross-section on one boundary, Q quantifies how this is stretched and squashed as the field lines are mapped to the other boundary. When Q is large, it is approximately given by the ratio of the largest to the smallest eigenvalue of the field line mapping Jacobian (Titov et al. 2002). It takes large values where neighboring field lines diverge and tends to infinity at separatrix surfaces. We use a convention wherein positive and negative Q correspond to closed and open field lines, respectively, i.e., negative Q denotes coronal holes; note that by definition $|Q| \geqslant 2$.

A map of Q at the inner radial boundary in relation to select magnetic field lines is shown in Figure 1(a). At a number of locations, pairs of magnetic field lines on both sides of the open/closed boundary are shown. The squashing factor at both the inner and outer radial boundaries as a function of polar and azimuthal angles is shown in Figures 1(b) and (c), respectively, with the polarity inversion line at the source surface marked in the latter plot. On the photosphere, a closed path of high

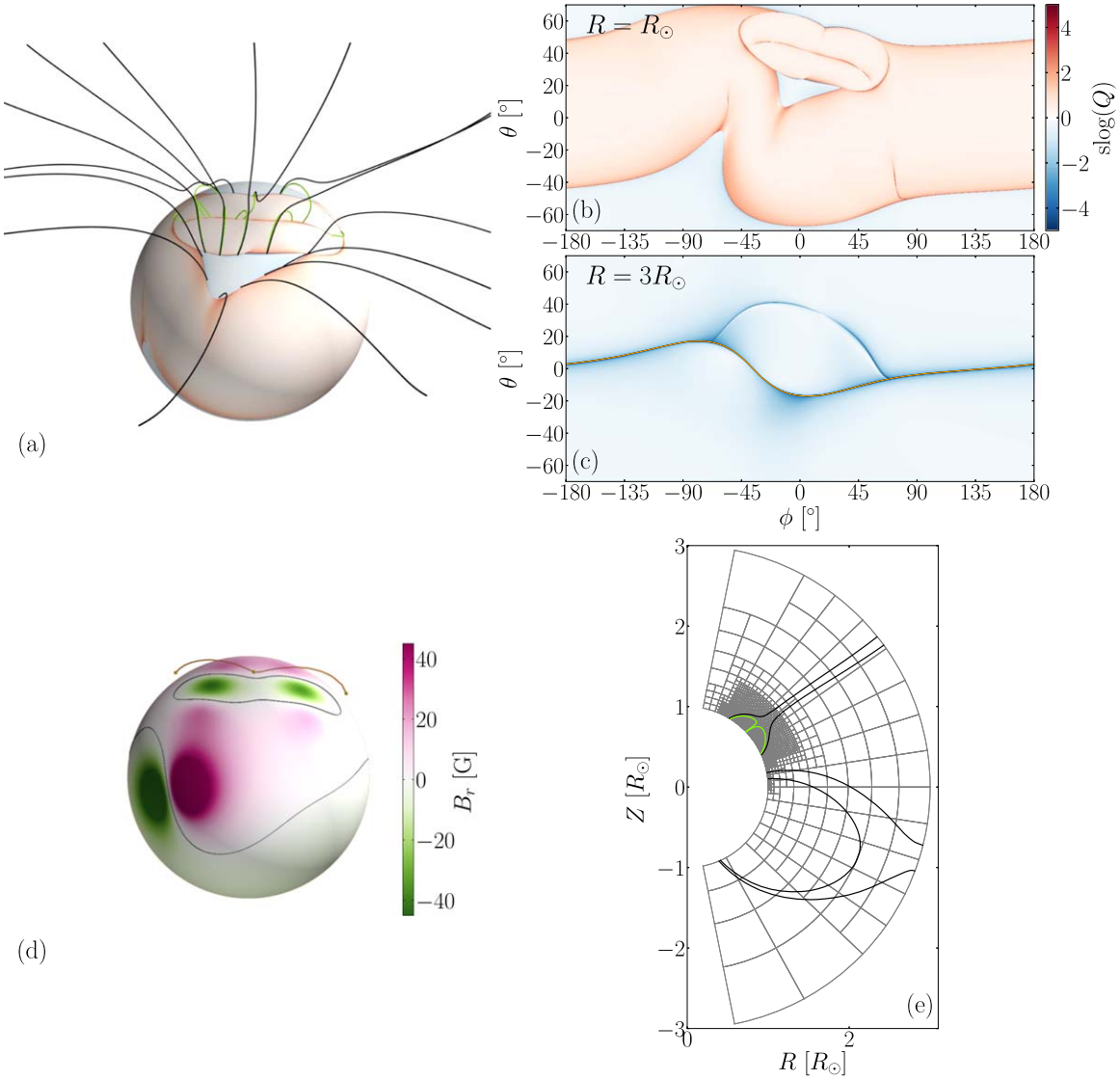

Figure 1. (a) The squashing factor Q at the photosphere with representative magnetic field lines at coronal hole boundaries and inside boundaries of the pseudostreamer. The closed magnetic field lines of the pseudostreamer "dome" are colored green, and all others are black. (b) Full Q map at the photosphere and (c) the source surface. By convention, positive and negative Q corresponds to closed and open field lines, respectively. The polarity inversion line at the source surface is indicated in (c) by the solid curve. The radial magnetic field B_r at the photosphere (d) with two polarity inversion lines indicated, the smaller corresponding to the parasitic polarity of the pseudostreamer. The three magnetic nulls, connected by the double bow-like separator line, are also shown. (e) Vertical slice through the simulation domain at $\phi = 0°$ showing projections of indicative magnetic field lines (black/green), corresponding to the pseudostreamer and helmet streamer, and blocks of the high-resolution simulation grid.

positive Q (located at $-50° \lesssim \phi \lesssim 50°; 20° \lesssim \theta \lesssim 60°$) is the photospheric footprint of the separatrix dome associated with the pseudostreamer. A disconnected line of high Q within this structure marks the footprint of the fan separatrix surface of one of the nulls that form the pseudostreamer. The counterpart to this—the open part of this fan separatrix surface—is what separates the flux of the two coronal holes, whose footprint at the source surface $r = 3R_\odot$ forms the arc that extends upwards from the polarity inversion line in the northern hemisphere (Figure 1(c)).

This geometry exhibits an asymmetric magnetic expansion out from the coronal hole. Field lines near the pseudostreamer remain largely parallel, while those closer to the equator increasingly diverge. This effect can be seen clearly in Figure 2, where a set of colored curves are shown at (a) the photosphere and (b) the source surface, respectively. Curves of a given color are connected by magnetic field lines, e.g., a field line passing through a point on the green curve at the photosphere then passes through the green curve at the source surface. The spacing of the curves is constant 1° at the photosphere by design, but becomes highly variable at the source surface. In particular, the portions of the curve in the upper center of the coronal hole become more tightly spaced (separation $< 1°$ at the source surface), while the lower portions are very widely spaced (separation $> 1°$). Figure 2 illustrates the well-known result that the so-called expansion factor is larger than radial near streamers, but smaller than radial near pseudostreamers (Riley & Luhmann 2012); exactly radial expansion would imply that the curves maintain their fixed angular separation everywhere. This will be important when we come to assess the effects of interchange reconnection at different locations around the coronal hole boundary, below.

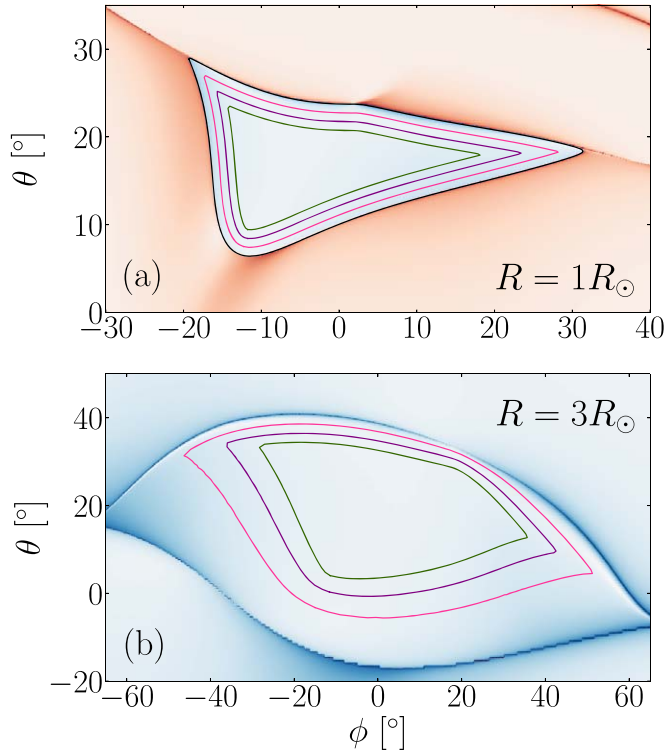

Figure 2. Detail of Q over (a) the coronal hole, with the open/closed boundary denoted by the black curve. The open magnetic field lines in this region map to (b) the source surface. The three colored curves are loci bounded by, and at a constant distance from, the open/closed boundary. The angular distances are 1°, 2°, and 3° at the photosphere, respectively. Field lines from each point on the curves are then followed to the source surface, where corresponding colored curves are also shown.

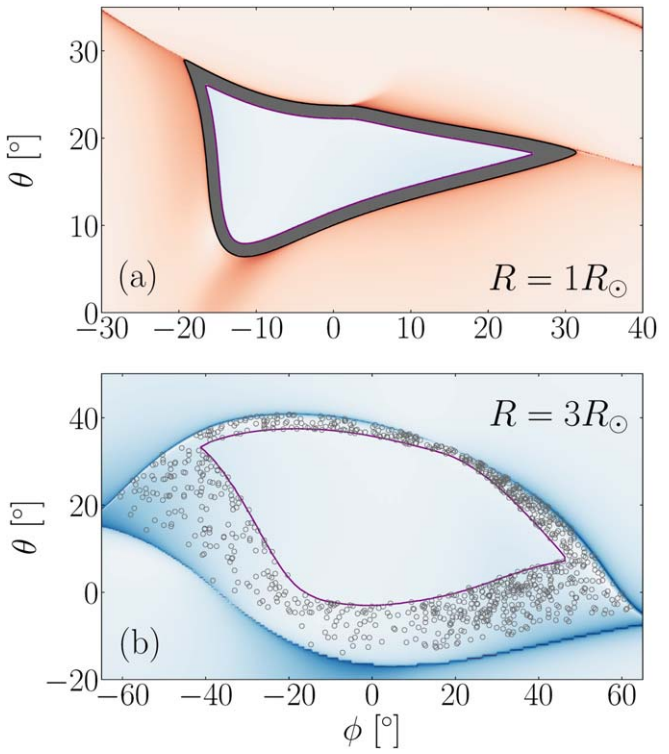

Figure 3. (a) Equilibrium Q map at the photosphere in the vicinity of the coronal hole. The black curve corresponds to the open/closed boundary, while the purple curve is offset inside by 1°.5—the approximate half-width of a supergranule. Between the two curves, shaded in gray, are footpoints of open magnetic field lines that we hypothesize to undergo interchange reconnection. (b) Corresponding Q map at the source surface. The gray circles correspond to the locations where a selection of field lines from the gray region in (a) intersect the source surface.

3. Possible Locations for Interchange Reconnection

As we have stated, interchange reconnection by its nature must necessarily occur across the open/closed boundary. This may be driven by many different process, but in order to explain the properties of a ubiquitous phenomenon such as the solar wind, we must consider driving processes that are occurring continuously on the Sun. One such driver is the solar granulation/supergranulation. Supergranules have a typical lateral extent of $L \sim 30$ Mm, an angular distance of $\Lambda \sim 3°$ at the equator on the photosphere (Rincon & Rieutord 2018). We could therefore expect magnetic field lines passing within approximately a supergranule half-width distance from the open/closed boundary to undergo interchange reconnection, within a typical supergranular turnover time. Before presenting results of fully dynamic simulations in the following sections, we consider different hypothetical outcomes. Consider first the initial static equilibrium field; suppose that interchange reconnection occurs in this geometry in response to the supergranular driving, and that a newly opened field line is equally likely to be found anywhere within one supergranule half-width from the open/closed boundary. In Figure 3 we randomly select open magnetic field lines passing through a region within 1°.5 of the open/closed boundary on the photosphere, and trace them to the source surface. Due to the magnetic geometry, the field expands more at the bottom of the coronal hole than at the pseudostreamer, so that the annular region within which newly opened field lines should be found in this hypothetical situation becomes wider toward the helmet streamer.

As an alternative to the above, consider the following. There is reason to believe that there might be preferential locations for interchange reconnection to occur based on the pattern of supergranulation. Thus, another possibility is that, instead of being spread uniformly throughout the supergranule half-width region, the footpoints of interchange-reconnected field lines are confined to narrow regions modulated by the width of each supergranule. In Figure 4, we consider idealized circular supergranules of width 3° centered on the open/closed boundary. Based on the hypothesis that reconnection is preferentially driven at the interfaces between supergranules, we extend lines out from the points where the circles touch and normal to the open/closed boundary as hypothetical newly opened flux regions. Field lines are then traced from these footpoints to the source surface. As in the example above, the magnetic expansion to the source surface is asymmetric; the additional modulation now adds a "finger"-like structure to the field lines that intersect the source surface. In this scenario, the slow wind would exhibit a "cellular" structure characterized by narrow filaments of recently reconnected field lines.

We proceed in the following to perform dynamic MHD simulations, in which we explore the extent to which each of the above hypotheses is borne out.

4. Interchange Reconnection Driven by a Surface Flow

4.1. Simulation Setup and Boundary Driving

We solved the set of equations of magnetohydrodynamics (MHD) using the Adaptively Refined Magnetohydrodynamic

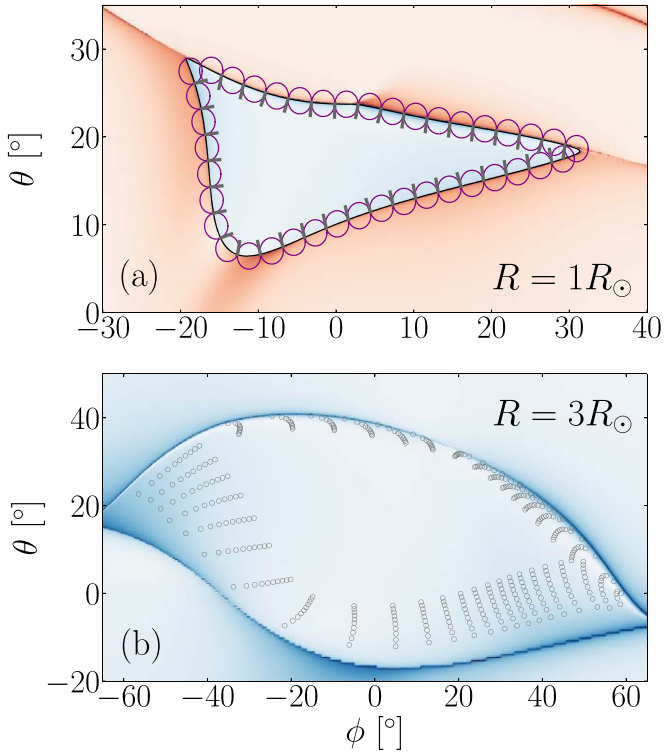

Figure 4. (a) Equilibrium Q map at the photosphere and (b) at the source surface. The black curve corresponds to the open/closed boundary. Each of the purple circles in (a) is centered on the open/closed boundary with a diameter of 3°, typical for a supergranule. The gray-shaded lines are located at the interfaces between circles, therefore also spaced by 3°, and 1°.5 in length. Field lines from these gray lines intersect the source surface at locations indicated by the gray circles in (b).

Solver (ARMS; DeVore 1991) in the absence of explicit resistivity. Non-ideal effects, such as magnetic reconnection, occur due to numerical resistivity inherent in any Eulerian MHD solver. Throughout the following simulations, we treated the plasma as isothermal at $T = 2$ MK. We allowed an initial simulation time of order 5000 s for the system to equilibrate, with $t = 0$ denoting the beginning of active driving as detailed below following the relaxation. This equilibration time was sufficient for plasma density to fully undergo slight redistribution, most notably following field lines under the pseudostreamer dome; the plasma velocity decays away by $t = 0$. For the simulations detailed below, the adaptive refinement was not required. Figure 1(e) shows a high-resolution grid (used for simulations in Section 5), where the gray lines inscribe blocks of $8 \times 8 \times 8$ grid points. For the illustrative simulation in this section, we use a coarser simulation grid with approximately one quarter the resolution. In both cases, the highest resolution is reserved for the pseudostreamer, where the magnetic geometry is most rapidly varying and where the dynamics of interchange reconnection must be accurately resolved; an intermediate grid spacing is used for the helmet streamer, where the length scale of variations is larger than the pseudostreamer; the lowest level of resolution is used for all other regions of the domain.

As a boundary condition at the lower (photospheric) boundary we impose incompressible, divergence-free flows of the form

$$v_\theta = v_0 \mathbb{G}(\theta - \theta_c)\mathbb{G}'(\phi - \phi_c)\frac{1}{\sin\theta} f(t) \tag{1}$$

$$v_\phi = -v_0 \mathbb{G}(\phi - \phi_c)\mathbb{G}'(\theta - \theta_c) f(t) \tag{2}$$

where v_0 is a constant, $\mathbb{G}(x) \equiv \exp(-cx^2)$ is the Gaussian function with scaling factor c, centered on θ_c and ϕ_c; $\mathbb{G}'(x) \equiv d\mathbb{G}/dx$. The product of the Gaussian function and its derivative result in a circular flow vanishing at its center and peaking at $(2c)^{-1/2}$ off-center. The time-dependent function $f(t)$ is smooth and typically sinusoidal, such that $|f(t)| \leqslant 1$. The constant v_0 is chosen to make the peak velocity of order 10 km s^{-1}.

Outside of the region where the above flows are prescribed, the boundary at $r = R_\odot$ is kept fixed by imposing $|\boldsymbol{v}| = 0$. This condition ties the field lines at the inner radial boundary. At the outer radial boundary, the radial velocity is set to zero (reflecting condition) and the transverse velocity is reduced through a half-slip boundary condition that sets its value to zero beyond the boundary. The dynamic magnetic field there is required to remain purely radial to maintain the source surface condition.

Due to the above-described boundary conditions, in the absence of reconnection in the coronal volume surface flows should reversibly deform the open/closed boundary, preserving the connectivity of each field line. Conversely, any deviation between the motion of plasma on the photosphere and the corresponding field line connectivity must be the result of reconnection in the corona.

In order to demonstrate these principles we first consider the dynamics that result from the application of a single rotational driving flow at the coronal hole boundary centered on $\theta = 24°$, $\phi = 8°$. The flow has a sinusoidal time dependence with the following properties:

$$f(t) = \frac{1}{2}\left[1 - \cos\left(\frac{2\pi(t - t_0)}{T'}\right)\right] \quad t_0 < t < \frac{T}{4} \tag{3}$$

$$f(t) = \sin\left(\frac{2\pi t}{T}\right) t \geqslant \frac{T}{4} \tag{4}$$

$$\int_{t_0}^{T} f dt = \int_{T}^{2T} f dt = 0 \tag{5}$$

where the period $T = 3000$ s. The constant T' is chosen such that Equation (5) holds; the start time $t_0 = T/4 - T'/2$ is small and negative. In effect, the first quarter period of the pure sinusoid has been replaced with the function $\frac{1}{2}[1 - \cos(2\pi(t - t_0)/T')]$ so that the flow begins with $df/dt = 0$, to avoid creating sharp transients due to suddenly switching on the flows. This time dependence results in a rotational flow in one sense, followed by a rotational flow in the opposite sense, as a result of which each point on the photosphere returns to its starting position after every period. Note that in practice the open/closed boundary itself will not return to its starting position after one period as a result of interchange reconnection. The other constants are chosen so that the flow is approximately 6° wide (in solar coordinates), with a velocity peaking in time and space at 40 km s^{-1}. This choice of angular width corresponds to 73 Mm at the solar equator, subtending ~100″ at 1 au. In the region of the largest displacement, the flow makes approximately one complete turn in the initial half of a given period, before reversing in the second half.

We note that the surface flow is of comparable size to a supergranule (perhaps around twice as large), and the surface

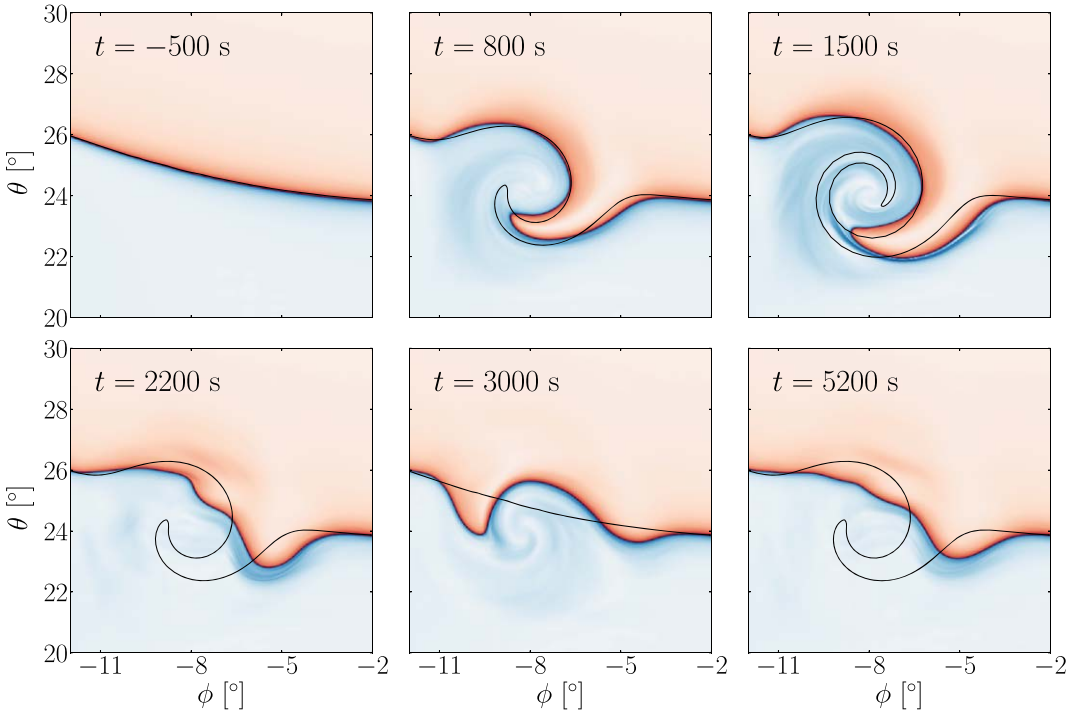

Figure 5. Maps of Q in the flow region at times indicated; the first five panels are separated by approximately a quarter of one period of rotation, $T = 3000$ s. The initial panel (before surface flows begin) is shown slightly earlier than $t = 0$, because the first quarter period is longer than the others (see details in text). Nonetheless, each point on the surface returns to its starting location an integer number of periods thereafter. The black curve corresponds to the open/closed boundary ideally advected by the surface flow.

motion in the following section is composed of multiple such flows. However, we note that this driver is not intended to mimic exactly observed photospheric driving patterns. Rather, its characteristics are representative of observed flows, in the sense that the random appearance and disappearance of granular/supergranular convection cells injects twist into the coronal field. The size of our surface flow is chosen to ensure that the driving region is resolved on the computational grid, while its particular incompressible form (having zero divergence) advects the plasma density and vertical magnetic field values unchanged. As with the spatial dependence, the peak velocity (scaled by the factor v_0) does not take photospheric values (being rather faster than typically observed flows), but it is representative of the Sun in that the timescale associated with the driving flow (∼3000 s for one-half rotation) is much longer than the dynamical timescale of the coronal volume (∼300 s for the Alfvén travel time along a typical field line beneath the pseudostreamer).

4.2. Coronal Evolution: Single Driver

The evolution of open and closed magnetic flux in the MHD simulation with driving as described above is shown in Figure 5. Maps of the squashing factor Q on the photosphere show the deformation of the open/closed boundary by the flow through a change in the distribution of Q (recall that closed field lines correspond to positive Q, colored red, while open field lines correspond to negative Q, colored blue). Shearing of magnetic field line footpoints can be seen through the formation of spirals of positive/negative Q. As mentioned above, in ideal MHD the field line footpoints, and therefore also the open/closed boundary, should return to their starting points after any integer number of driving periods. However, the open/closed boundary is unlikely to return to its original shape in the present non-ideal simulations due to the formation of current sheets. At each time we indicate with a black curve the expected position of the open/closed boundary under ideal evolution (i.e., under pure advection by the driving flow). We find that the observed open/closed boundary (as determined by tracing magnetic field lines at each instant in time, and visualized with the Q map) deviates from the ideal case at all times, and moreover does not return to its starting position. The relatively small deviations at early times may be ascribed to the relatively coarse grid resolution used in this calculation. The much larger deviations at later times can only be explained by magnetic reconnection occurring in the corona; similar patterns were reported previously by Higginson et al. (2017b).

We classify each point on the photosphere based upon whether the connectivity (classified either open or closed) behaves as expected from ideal motion, or deviates due to reconnection of the corresponding field line. Such a classification map at $t = 800\ \mathrm{s} \simeq 0.25T$ is shown in Figure 6(c); it can be compared to the map of Q at the photosphere together with the curve indicating the ideal open/closed boundary position in Figure 6(a). It is worth noting that such a map based purely on the open/closed connectivity does not detect changes of connectivity *within* either the closed- or open-field regions. Here, we are focused on interchange reconnection and are interested only in whether a given field line footpoint on the photosphere remains an open footpoint (green in Figure 6(c)), remains closed (brown), is reconnected from open to closed (pink), or is reconnected from closed to open (gray).

In Figure 6(b) we show a map of Q at the source surface. A sample of reconnected open field lines (gray in the classification) are traced up from the photosphere; the locations where

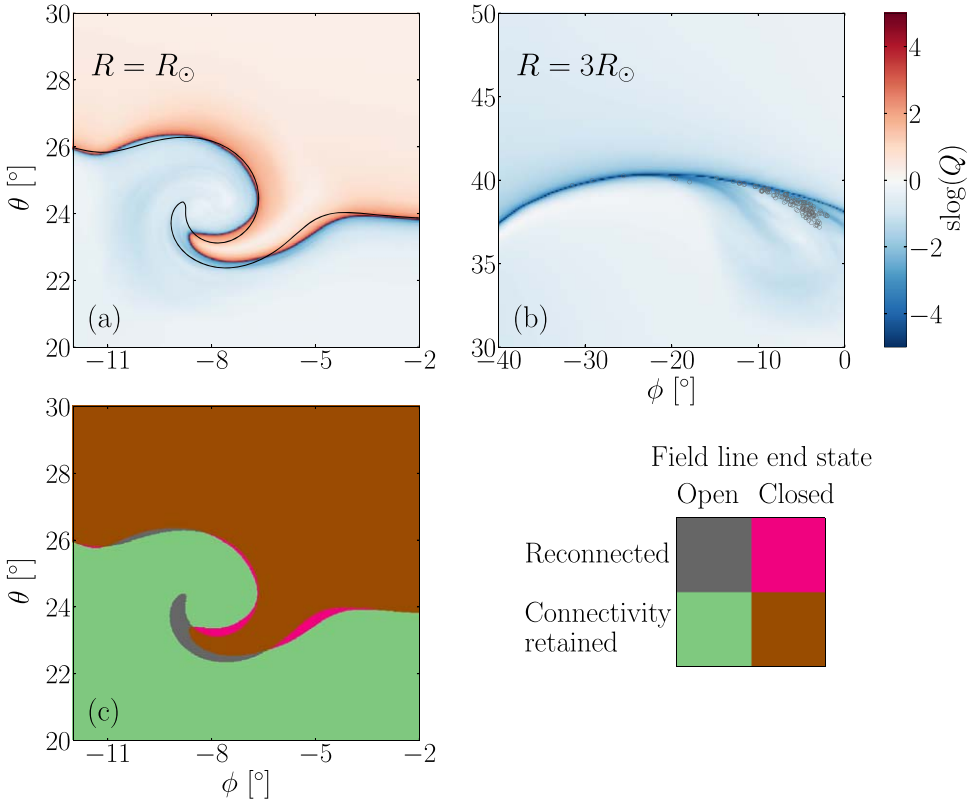

Figure 6. (a) Map of Q at $t = 800$ s at the photosphere. The black curve indicates where the open/closed boundary would lie under pure ideal advection (no coronal reconnection). (b) Map of Q at the source surface; the locations where a select number of open non-advected field lines intersect the source surface are indicated by the hollow circles. (c) Classification in the changes of field line connectivity by color as labeled.

they intersect the source surface are indicated by hollow circles. Put another way, field lines intersecting the hollow circles are connected to photospheric footpoints that were previously in the closed-field region. Outflow along these field lines, therefore, is expected to contribute closed-corona plasma to the solar wind.

We illustrate the currents (normalized to the magnetic field) associated with reconnection in Figure 7. We select a point on the photosphere which is initially well within the closed-field region, meaning that under ideal circumstances the associated field line should remain closed regardless of any subsequent surface motion. This is still the case at $t = 799$ s, when the point is located near $\theta \approx 22.^\circ9$, $\phi \approx -8.^\circ4$, just within the brown region in Figure 6 (closed, connectivity retained). We advect the point under the influence of the surface flow for 1 s (the time is then exactly that shown in Figure 6) at which time the associated field line has become open. We deduce that the magnetic field line associated with this moving point has reconnected in the brief intervening time period. Projections of the field lines associated with this point at both times are also shown in Figure 7.

Reconnecting field lines are closely aligned with the currents flowing along the boundary of the pseudostreamer dome. The two example field lines in Figure 7 diverge near the separator line connecting null points in the pseudostreamer configuration, through which the interchange reconnection takes place. Curves indicating the magnetic field strength $|\boldsymbol{B}|$ and the normalized parallel current $\boldsymbol{J}\cdot\boldsymbol{B}/|\boldsymbol{B}|^2$ along the two field lines are also shown. The two field lines diverge at a minimum in magnetic field strength (indicative of the separator) in a region where the parallel current peaks. This confirms that the

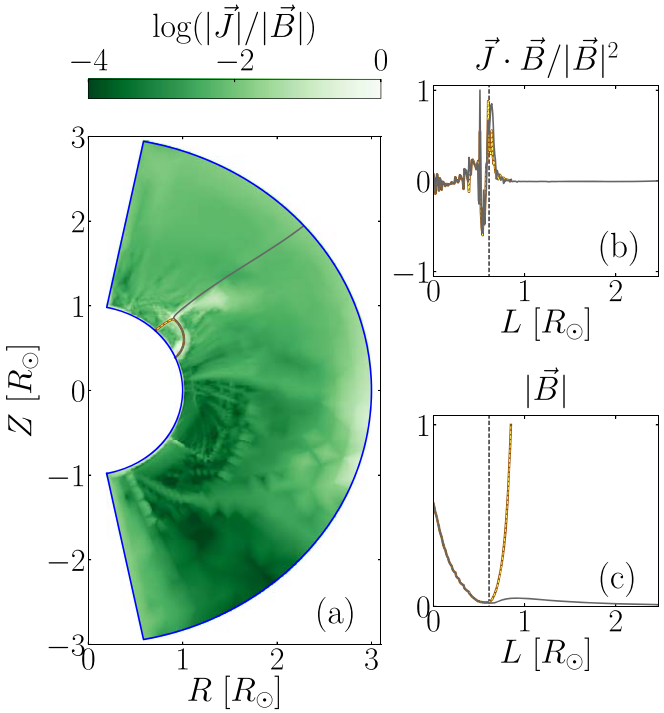

Figure 7. (a) Vertical slice through the simulation domain at $\phi = -8.^\circ4$ showing $|\boldsymbol{J}|/|\boldsymbol{B}|$ and two field lines with a common (moving) footpoint at $t = 799$ s (brown, dashed) and $t = 800$ s (gray). The field lines reconnect as the footpoint crosses the open/closed boundary. (b) The normalized parallel current and (c) the magnetic field strength as functions of path length L along the field lines. The dashed line marks the path length at which the two field lines diverge.

reconnection at the pseudostreamer proceeds as expected: in such a configuration with 3D coronal nulls the current is expected to accumulate at the null points (and separators, should they exist), leading to reconnection across the separatrix surface (e.g., Antiochos 1996; Pontin et al. 2007).

5. Dynamical Deformation of the Coronal Hole Boundary

We now consider a more complex and realistic surface motion in which boundary flows are distributed across the photosphere in the vicinity of the coronal hole (rather than being present only in a single, isolated patch). We use the high-resolution simulation grid shown in Figure 1 and impose 44 circular surface flows with the same size as above, but staggered in time and spatial location. For simplicity, each flow has the identical spatial structure given in Equations (1) and (2). We select the center (ϕ_c, θ_c) of each driving flow to be in or around the coronal hole, and set the velocity scale factor v_0 of each flow to achieve peak velocities in the range 8 to 16 km s^{-1}. In addition, for every flow with a given value of v_0 there is an opposing flow with value $-v_0$, which means that the net magnetic helicity injection into the domain is approximately zero.

The flows each have a very similar time dependence, differing only by an offset. The time-dependent function for flow i is given by

$$f_i(t) = \frac{1}{2}\left[1 - \cos\left(\frac{2\pi(t - t_i)}{T}\right)\right] \qquad t_i < t < t_i + T \qquad (6)$$

where the period $T = 2000$ s for all flows. The start times t_i are staggered relative to one another, but largely form two groups: the first with t_i between 0 and 1000 s, the second between 2000 and 3000 s. Note that unlike the one-flow case described in Section 4.2, no single flow returns points on the photosphere back to their original locations (i.e., the rotation is in one sense and does not subsequently reverse at the same location).

As before, we follow the MHD evolution in the domain in response to these driving flows. Currents are again found to accumulate in the vicinity of the pseudostreamer, as well as the helmet streamer, driving interchange reconnection. We analyze this interchange of flux by plotting maps of the squashing factor Q in Figure 8 at selected times. The hypothetical ideal motion of the open/closed boundary (under pure advection by the surface flows) is indicated by the black curve at the photosphere. The true motion of the open/closed boundary deviates from the case of an ideal corona, particularly in regions where its displacement is high. As illustrated in Figure 2, the open field lines from near the pseudostreamer are tightly bunched at the source surface ($R = 3R_\odot$), while the open field lines from the lower part of the coronal hole diverge to fill a large area at the source surface. Consequently, we see that surface flows at the pseudostreamer boundary have only localized effects on the Q map at the source surface. On the other hand, the surface flows away from the pseudostreamer produce large-scale, extended features resembling "fingers" at the source surface. Flows away from the open/closed boundary create spiral structures in the Q map (visible at the photosphere for both open and closed field lines, and at the source surface only for open lines), but they do not stimulate interchange reconnection.

We display the connectivity map, constructed as described above, in Figure 9, classifying the footpoints of magnetic field lines on the photosphere based on whether they are open or closed, and whether they have retained their connectivity or reconnected. We indicate the locations where reconnected open field lines (corresponding to gray footpoints) intersect the source surface with gray circles; these points coincide with the "fingers" of high Q. Intuitively, this result can be understood through Figure 4: the surface flows driving interchange reconnection are effectively modulated (by approximately 6° in this case) and hence their signatures at the source surface are similarly spaced.

For the changes in field line connectivity to represent true interchange reconnection, the total magnetic flux through the reconnected closed/open (pink/gray) regions must be equal; numerical integration confirms this to be the case. Furthermore, the reconnected open flux is indicative of the volume of plasma released into slow solar wind: at $t = 5000$ s, this forms 6% of the total flux underneath surface flows adjacent to the open/closed boundary. We note that this figure may be dependent on a number of factors, such as the driving speed, the grid resolution, and the degree of pre-existing stress in the field. Furthermore, the denominator in this ratio is dependent strongly on the flux distribution at the flow locations.

6. Conclusions

In our simulations, we have observed and quantified interchange reconnection in a pseudostreamer geometry. The dynamics are driven by flows at the photosphere resembling supergranules, with the flows ~70 Mm wide occurring at timescales on the order of hours. The interchange reconnection itself is found to occur at the nulls and separators at the top of the pseudostreamer, consistent with observations of bright stalks atop pseudostreamers. At heights below the pseudostreamer dome apex, the photospheric flows introduce considerable deformation into the open–closed boundary prior to interchange reconnection, leading to a corrugation of this flux surface. This corrugation inherits the length scales from the driving flow, and the complexity should be determined by (averaged over space and time) the balance between the driving flows (that typically increase the corrugation) and dissipation-induced interchange reconnection (that typically is expected to decrease the corrugation). This continuous, time-dependent deformation of the open–closed boundary is a natural ingredient in explaining the ragged or fuzzy boundaries of coronal holes.

The most striking result of our simulations is that newly opened magnetic field lines are distributed on the source surface in finger-like filaments. This is driven by a preferential occurrence of interchange reconnection in the lanes between our "supergranular" driving regions, and suggests that the photospheric network should be expected to create an imprint in the heliosphere. Given that the newly opened field lines are likely to vent plasma, contributing to the slow solar wind, we propose that these filaments should be observable in in situ observations from the PSP. In fact, Borovsky (2008) has presented evidence for a supergranular imprint on solar wind structure that persists as far out as 1 au.

Rapid field line expansion at the coronal hole periphery means that newly opened field lines are found within a substantial portion of the coronal hole at the source surface (Figure 9). We note from this figure that the angular extent of the newly opened field lines is larger at the helmet streamer boundary, the heliospheric current sheet, than at the pseudostreamer boundary, the S-Web arc. This effect is somewhat

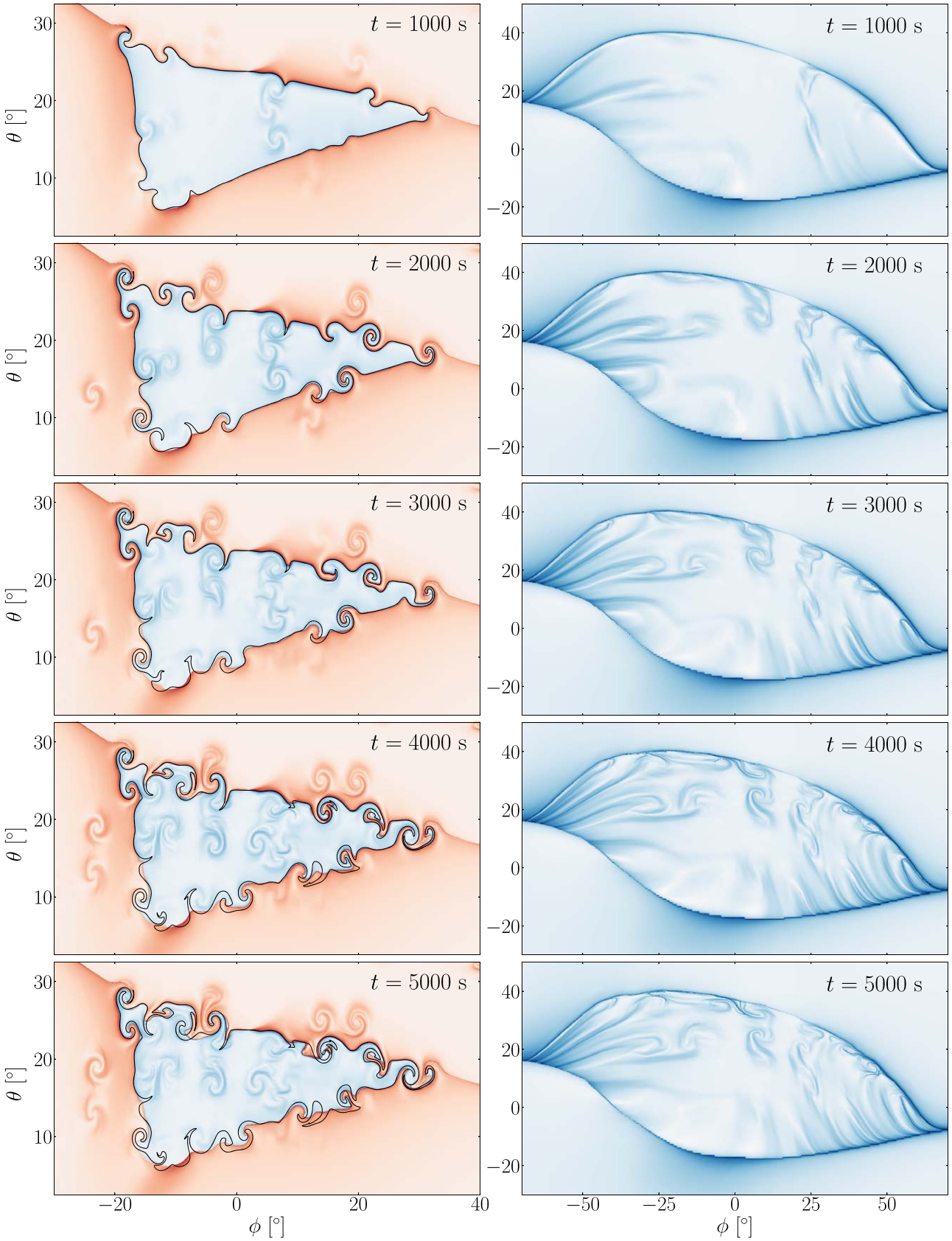

Figure 8. Map of Q across the coronal hole at times indicated at the photosphere (left column) and source surface (right column). At the photosphere, the black curve indicates where the open/closed boundary would lie under pure ideal advection (were there to be no reconnection in the simulation domain).

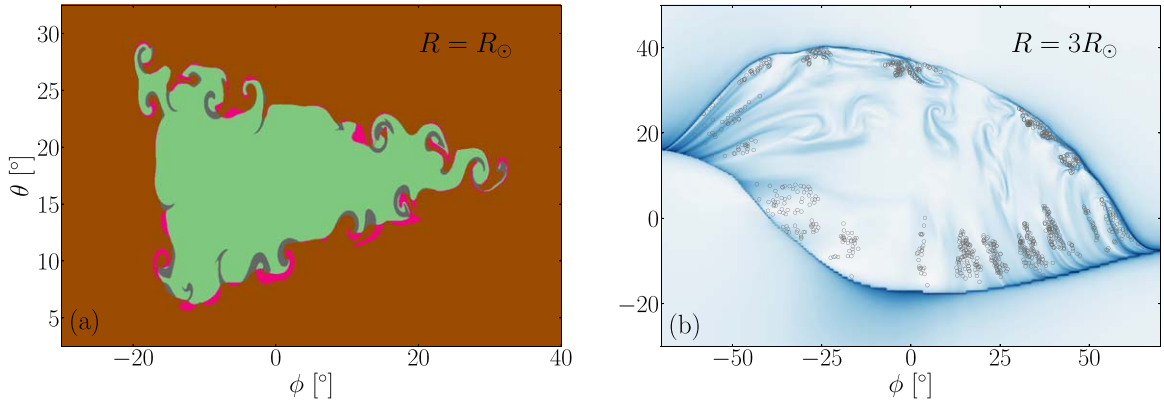

Figure 9. (a) Map of field line connectivity for the case of multiple surface flows at $t = 5000$ s. The color convention is identical to Figure 6. (b) Map of Q at the source surface. Positions where selected field lines that have been reconnected from closed to open intersect the source surface are indicated by circles.

exaggerated by our use of the source surface model, which has a non-uniform distribution of normal flux at the source surface. Ulysses observations have found the radial flux in the heliosphere is observed to be approximately uniformly distributed over a radial surface, at least, at 1 au and beyond (Smith & Balogh 1995). Of course, at the heliospheric current sheet the radial field vanishes irrespective of distance from the Sun, so there is always an enhanced expansion there, even though it is unlikely to be as pronounced as shown in Figure 9.

To obtain an approximate scale for the filaments of newly opened flux, suppose that they have size L_f perpendicular to the corresponding S-Web arc, and width w_f in the direction parallel to the S-Web arc. Then we expect $L_f \sim r_s \sqrt{f(r)}$ where r_s is a supergranule radius and $f(r)$ is the usual (areal) expansion factor. In our simulations we calculated that around 6% of the flux driven by supergranular flows spanning the open–closed boundary undergoes interchange reconnection in a period of 5000 s. This is on the order of the "outgassing" time for a newly reconnected field line. Thus, $w_f \sim 0.06 \times r_s \times G \times \sqrt{f(r)}$, where G is a geometrical factor that takes account of the increased (average) magnetic field strength in the lanes between supergranules compared to their centers of supergranules (Rincon & Rieutord 2018).

The result that only 6% of the driven flux undergoes interchange merits some discussion. This number implies that most of the imposed flow >90% has resulted in distortion of the open–closed boundary and, in fact, it is evident from Figure 9 that a large distortion of the initially smooth boundary has occurred. The key question is whether due to the action of ceaseless driving everywhere, as in the actual photosphere, this boundary eventually achieves a statistical steady-state or as suggested by some models, such as Fisk & Zurbuchen (2006), no well-defined boundary exists, because the open flux continuously diffuse into the closed. If the former, then eventually the amount of interchange reconnection must equal the rate at which flux is driven through the time-averaged boundary. In this case we expect that all the flux within one supergranular cell of the boundary would undergo interchange and contribute to the slow wind. On the other hand, if the Fisk model is correct, then the amount of interchange could be much larger depending on how much flux has diffused in the closed, and the rate at which this flux diffuses. Note also that we have applied only large-scale flows representative of supergranulation; super-imposed on this pattern is expected a smaller-scale imprint of the granulation, which could aid in the diffusion. Our results above show no evidence of a diffusive process; the boundary becomes highly distorted but remains topologically well-connected. It remains to be seen, however, if the boundary remains well-connected for long-term driving and, if so, the topology of the time-averaged state.

We finish with a note of caution. The simulations presented here have a closed domain, meaning that an explicit outflow of solar wind is absent. This issue will be addressed in future simulations, which will include plasma flows through open boundaries and a greatly extended domain in the radial direction to capture the effects of a true solar wind. An expanded domain would allow the analytical techniques presented here to be used with greater confidence, as the extended field lines in the larger domain would be less constrained by line-tying with the current half-slip outer radial boundary condition. We expect that our results above for interchange reconnection at the pseudostreamer boundary will be largely unchanged by the use of an expanded domain, because this reconnection occurs well below the source surface. Caution, however, should be used in interpreting the dynamics at the helmet streamer portion of the open–closed boundary in the simulations described herein. Due to boundary conditions at the source surface the helmet streamer is unable to contract/expand and, therefore, the effects of field line opening and closing are not included in our model. Future larger-scale simulations that include the heliospheric current sheet will allow for a much more robust analysis of the helmet streamer dynamics.

This work was performed using resources provided by the Cambridge Service for Data Driven Discovery (CSD3) operated by the University of Cambridge Research Computing Service, provided by Dell EMC and Intel using Tier-2 funding from the Engineering and Physical Sciences Research Council (capital grant EP/P020259/1), and DiRAC funding from the Science and Technology Facilities Council. V.A. is supported by the Science and Technology Facilities Council, grant number ST/S000267. R.S. is supported by the Office of Naval Research 6.1 basic research program. S.K.A. and C.R.D. were supported by the NASA HSR, LWS, and ISFM Programs.

Appendix
Magnetic Dipole Configuration

The strengths, locations, and orientations of six magnetic dipoles are given in Table 1. The dipole position is given in spherical coordinates R, θ, ϕ, consistent with the system

Table 1
The Positions and Magnetic Moments of The Magnetic Dipoles Making up The Equilibrium Magnetic Field Configuration

R (cm)	θ (deg)	ϕ (deg)	m_R	m_θ	m_ϕ
0	0	0	1.715×10^{27}	0	0
5.25×10^{10}	0	−36	0	0	5.359×10^{26}
5.25×10^{10}	52.2	−10.8	0	-1.438×10^{26}	0.719×10^{26}
5.25×10^{10}	41.4	39.6	0	-1.198×10^{26}	0.599×10^{26}
5.25×10^{10}	39.6	−14.4	0	1.438×10^{26}	-0.719×10^{26}
5.25×10^{10}	28.8	36	0	1.198×10^{26}	-0.599×10^{26}

Note. The magnetic moments are given in Gaussian units of G cm^3.

reported here (see above for details). The dipole moment is also resolved in this coordinate system, so that $m_R \equiv \boldsymbol{m}.\hat{R}$, $m_\theta \equiv \boldsymbol{m}.\hat{\theta}$, $m_\phi \equiv \boldsymbol{m}.\hat{\phi}$, which are given in the Gaussian system in units of G cm^3. The first entry is for the global solar dipole, which is set up to achieve a field $B = 10$ G at the poles on the photosphere. Note that none of the other dipoles is oriented in the radial direction.

ORCID iDs

V. Aslanyan https://orcid.org/0000-0003-3704-4229
D. I. Pontin https://orcid.org/0000-0002-1089-9270
P. F. Wyper https://orcid.org/0000-0002-6442-7818
R. B. Scott https://orcid.org/0000-0001-8517-4920
S. K. Antiochos https://orcid.org/0000-0003-0176-4312
C. R. DeVore https://orcid.org/0000-0002-4668-591X

References

Abbo, L., Ofman, L., Antiochos, S. K., et al. 2016, SSRv, 201, 55
Altschuler, M. D., & Newkirk, G. 1969, SoPh, 9, 131
Antiochos, S. K. 1996, in ASP Conf. Ser. 95, Solar Drivers of the Interplanetary and Terrestrial Disturbances, ed. K. S. Balasubramaniam, S. L. Keil, & R. N. Smartt (San Francisco, CA: ASP), 1
Antiochos, S. K., Mikić, Z., Titov, V. S., Lionello, R., & Linker, J. A. 2011, ApJ, 731, 112
Borovsky, J. E. 2008, JGRA, 113, A08110
Cranmer, S. R. 2009, LRSP, 6, 3
Crooker, N. U., Gosling, J. T., & Kahler, S. W. 2002, JGRA, 107, 1028
DeVore, C. R. 1991, JCoPh, 92, 142
Fisk, L. A., & Zurbuchen, T. H. 2006, JGRA, 111, A09115
Higginson, A. K., Antiochos, S. K., DeVore, C. R., Wyper, P. F., & Zurbuchen, T. H. 2017a, ApJ, 837, 113
Higginson, A. K., Antiochos, S. K., DeVore, C. R., Wyper, P. F., & Zurbuchen, T. H. 2017b, ApJL, 840, L10
Kahler, S. W., & Hudson, H. S. 2002, ApJ, 574, 467
Karpen, J. T., Antiochos, S. K., & DeVore, C. R. 2012, ApJ, 760, 81
Masson, S., McCauley, P., Golub, L., Reeves, K. K., & DeLuca, E. E. 2014, ApJ, 787, 145
Platten, S. J., Parnell, C. E., Haynes, A. L., Priest, E. R., & Mackay, D. H. 2014, A&A, 565, A44
Pontin, D. I., Bhattacharjee, A., & Galsgaard, K. 2007, PhPl, 14, 052106
Pontin, D. I., & Wyper, P. F. 2015, ApJ, 805, 39
Riley, P., & Luhmann, J. G. 2012, SoPh, 277, 355
Rincon, F., & Rieutord, M. 2018, LRSP, 15, 6
Schatten, K. H., Wilcox, J. M., & Ness, N. F. 1969, SoPh, 6, 442
Scott, R. B., Pontin, D. I., & Wyper, P. F. 2019, ApJ, 882, 125
Scott, R. B., Pontin, D. I., Yeates, A. R., Wyper, P. F., & Higginson, A. K. 2018, ApJ, 869, 60
Smith, E. J., & Balogh, A. 1995, GeoRL, 22, 3317
Tassev, S., & Savcheva, A. 2017, ApJ, 840, 89
Titov, V. S., Hornig, G., & Daémoulin, P. 2002, JGR, 107, 1164
Titov, V. S., Mikić, Z., Linker, J. A., Lionello, R., & Antiochos, S. K. 2011, ApJ, 731, 111
Viall, N. M., & Borovsky, J. E. 2020, JGRA, 125, e26005
Wang, Y.-M., Sheeley, N. R., Jr., & Rich, N. B. 2007, ApJ, 658, 1340
Wyper, P. F., DeVore, C. R., Karpen, J. T., & Lynch, B. J. 2016, ApJ, 827, 4
Zirker, J. B. 1977, RvGSP, 15, 257